Since January 2020 Elsevier has created a COVID-19 resource centre with free information in English and Mandarin on the novel coronavirus COVID-19. The COVID-19 resource centre is hosted on Elsevier Connect, the company's public news and information website.

Elsevier hereby grants permission to make all its COVID-19-related research that is available on the COVID-19 resource centre - including this research content - immediately available in PubMed Central and other publicly funded repositories, such as the WHO COVID database with rights for unrestricted research re-use and analyses in any form or by any means with acknowledgement of the original source. These permissions are granted for free by Elsevier for as long as the COVID-19 resource centre remains active.

Biosensors and Bioelectronics 208 (2022) 114198

Contents lists available at ScienceDirect

Biosensors and Bioelectronics

journal homepage: www.elsevier.com/locate/bios

Rapid and sensitive detection of viral particles by coupling redox cycling and electrophoretic enrichment

Derrick Butler [a,b], Aida Ebrahimi [a,b,c,d,*]

[a] Department of Electrical Engineering, The Pennsylvania State University, University Park, PA, 16802, USA
[b] Materials Research Institute, The Pennsylvania State University, University Park, PA, 16802, USA
[c] Department of Biomedical Engineering, The Pennsylvania State University, University Park, PA, 16802, USA
[d] Center for Biodevices, The Pennsylvania State University, University Park, PA, 16802, USA

ARTICLE INFO

Keywords:
Electrochemical sensor
Virus
Redox cycling
Electrophoresis
Particle collision

ABSTRACT

The COVID-19 pandemic has highlighted the need for rapid, low-cost, and sensitive virus detection platforms to monitor and mitigate widespread outbreaks. Electrochemical sensors are a viable choice to fill this role but still require improvements to the signal magnitude, especially for early detection and low viral loads. Herein, finite element analysis of a novel biosensor concept for single virion counting using a generator-collector microelectrode design is presented. The proposed design combines a redox-cycling amplified electrochemical current with electrophoresis-driven electrode-particle collision for rapid virus detection. The effects of experimental (*e.g.* scan rate, collector bias) and geometric factors are studied to optimize the sensor design. Two generator-collector configurations are explored: a ring-disk configuration to analyze sessile droplets and an interdigitated electrode (IDE) design housed in a microchannel. For the ring-disk configuration, we calculate an amplification factor of ~5 and collector efficiency of ~0.8 for a generator-collector spacing of 600 nm. For the IDE, the collector efficiency is even larger, approaching unity. The dual-electrode mode is critical for increasing the current and electric field strength. As a result, the current steps upon virus capture are more than an order of magnitude larger compared to single-mode. Additionally, single virus capture times are reduced from over 700 s down to ~20 s. Overall, the frequency of virus capture and magnitude of the electrochemical current steps depend on the virus properties and electrode configuration, with the IDE capable of single virus detection within seconds owing to better particle confinement in the microchannel.

1. Introduction

Prompt and accurate detection of viruses is critical for upholding public safety and minimizing widespread outbreaks of infectious diseases.[(Caygill et al., 2010; Fox, 2007)] This is especially relevant in the backdrop of the current COVID-19 pandemic – caused by the Severe Acute Respiratory Syndrome Coronavirus 2 (SARS-CoV-2)[(Baig, 2021)] – which is responsible for more than 428 million infections and 5.9 million deaths globally at the time of writing this article.[(Johns Hopkins University, 2022)] Although the COVID-19 pandemic has been the most widespread in recent history, outbreaks caused by other viruses, such as influenza, dengue, human immunodeficiency virus (HIV), and Ebola place additional stress on the global healthcare system. [(Kisely et al., 2020)] Widespread testing is a cornerstone of the effort to mitigate the devastating impact of present and future pandemics. Simple-to-use, sensitive, and rapid diagnostics that can be manufactured at relatively low cost and at a large scale are critical to better monitor the spread of infection and minimize the burden on healthcare systems.

Current strategies for detecting viral infections include polymerase chain reaction (PCR), reverse transcription polymerase chain reaction (RT-PCR), [(Bustin, 2000)] enzyme linked immunosorbent assays (ELISA), [(Voller et al., 1976)] isothermal amplification, [(Kievits et al., 1991; Ito et al., 2006)] and immunochromatography, [(Arai et al., 1999)] among others. While effective, many of these techniques require significant overhead and have limited operational capacity outside of clinical settings. Therefore, electrochemical sensors are becoming increasingly used for virus detection, [(Zhao et al., 2021)] especially in point-of-need (PON) applications that require prompt results, minimal sample preparation, and simple-to-use equipment.[(Caygill et al., 2010)] The operating principle typically relies on changes in the current

* Corresponding author. 111J Electrical Engineering West, University Park, PA, 16802, USA.
E-mail address: sue66@psu.edu (A. Ebrahimi).

https://doi.org/10.1016/j.bios.2022.114198
Received 23 December 2021; Received in revised form 24 February 2022; Accepted 16 March 2022
Available online 18 March 2022
0956-5663/© 2022 Elsevier B.V. All rights reserved.

or impedance at the electrode-electrolyte interface from a redox molecule as virus particles attach to the electrode surface.[(Caygill et al., 2010)] To increase the appeal of electrochemical sensors for PON applications, electrode miniaturization is actively being pursued to further reduce sample volume requirements, [(Vishnu et al., 2020)] improve spatial resolution, especially in sensor arrays, [(Wolfrum et al., 2016)] and explore previously inaccessible regions, such as the interior of individual cells.[(Guo et al., 2022)] However, due to the reduced capture area of miniaturized electrochemical sensors, the number of virions reaching the sensor is reduced. In an effort to improve the sensitivity, redox cycling can be employed.[(Wolfrum et al., 2016; Ma et al., 2013; Lee et al., 2018)]

Redox cycling leverages two independently biased working electrodes spaced in close proximity to one another. One electrode is biased above the formal potential (E^0) of the redox probe while the other is biased below, allowing the oxidized and reduced species to cycle between the electrodes.[(Bard and Faulkner, 2001)] This recycling amplifies the current and can lead to increased signal-to-noise ratios. As a result, redox cycling has been applied for the detection of a variety of analytes, including dopamine, [(Kätelhön et al., 2010)] catechol, [(Wolfrum et al., 2008)] ferri/ferrocyanide ($[Fe(CN)_6]^{3-/4-}$), [(Ma et al., 2013; Straver et al., 2012)] paracetamol, [(Goluch et al., 2009; Paixão et al., 2006)] nitrate/nitrite, [(Gross et al., 2015)] and clozapine [(Ben-Yoav et al., 2014; Winkler et al., 2017)] with amplification factors ranging from 1 to 2 to well over 6000.[(Wolfrum et al., 2016; Straver et al., 2012)] For example, Lee et al. recently demonstrated an amperometric redox cycling sensor based on an interdigitated electrode (IDE) design for detecting the hepatitis B virus surface antigen.[(Lee et al., 2018)] The sensor was combined with a commercial ELISA kit and demonstrated more than 10-fold higher sensitivity in dual-electrode mode compared to single-electrode mode, highlighting the potential of this technique for improving virus detection.

The charged surface of virions makes them prime candidates for electrophoretic manipulation. The surface charge is highly dependent on the medium properties, especially pH. Typically, viruses have an isoelectric point below pH 7, making them negatively charged at physiological pH values.[(Michen and Graule, 2009)] As a result, the virus particles are preferentially attracted to the anode where they can attach to the electrode surface. Such particle collisions can alter the electrochemical landscape of the electrode and cause detectable changes in the local capacitance [(Hellberg et al., 2002, 2005)] and charge transfer. [(Rees et al., 2004; Clegg et al., 2006; Xiao and Bard, 2007; Xiao et al., 2008)] The particle collision method has been applied in the detection of bacteria, such as *Escherichia coli*, [(Lee et al., 2016; Frkonja-Kuczin et al., 2018)] mammalian cells, [(Dick, 2016)] and viruses, [(Dick et al., 2016)] with the ultimate end goal being single entity detection in as little time as possible.[(Goines and Dick, 2020)]

In this work, we present the finite element analysis (FEA) of a novel biosensor concept that combines the advantages of redox cycling and electrophoretic enrichment for rapid detection and counting of single virus particles. The detection scheme is based on a current quenching strategy whereby the electrochemical current from the cyclic reduction and oxidation of a redox couple ($[Fe(CN)_6]^{3-/4-}$ as model) is suppressed as virus particles are captured at the electrode surface. Similar "current blocking" strategies have been reported previously using individual microelectrodes.[(Quinn et al., 2004; Boika et al., 2012; Lebègue et al., 2015)] Here, two mushroom-like, generator-collector microelectrode configurations, a ring-disk configuration and IDE design, are demonstrated. The ring-disk configuration could be suitable for application in digital microfluidic platforms, whereas the IDE configuration is more often utilized within microfluidic channels. The mushroom-like design can be achieved based on a scalable, templated electrodeposition strategy and yields tunable geometries that improve the redox cycling characteristics through reduced generator-collector spacing. Such designs have been experimentally reported recently [(Chen et al., 2015; Chandramohan et al., 2016; Cerquido et al., 2018)] and show potential for biosensing applications. We explore various design parameters, including electrode geometry, testing geometry (*e.g.* microchannel, droplet), and experimental conditions (*e.g.* voltammetric scan rate, electrolyte concentration), to better understand their effect on the amplification factor (Γ) and collector efficiency (η) and optimize the proposed platform. Depending on the experimental parameters and electrode geometry, single virus collisions can be detected on the order of seconds. The computational results herein provide design rules and assist in guiding the experimental development of biosensors suitable for single particle counting, with potential applications including virus detection, immunoassays, and nanoparticle-based molecular diagnostics.

2. Methods

2.1. Model geometry

The generator-collector ring-disk configuration consists of two concentric 3D microelectrodes, an inner "disk" and outer "ring" for the droplet-based design (Fig. 1). For this configuration, a 1 μl hemispherical droplet (unless otherwise specified) containing 1 mM $[Fe(CN)_6]^{4-}$ in a supporting KCl electrolyte is used. For the interdigitated electrode (IDE) design (Fig. 1), two electrodes with comb-like fingers are placed in an alternating pattern and contained within a microfluidic channel (not shown). At the top of all electrodes is a mushroom-like cap that could be formed by a template-driven over-electrodeposition.[(Chen et al., 2015)] The width of the electrode base (w_e) is 2 μm which is within the resolution of standard photolithography methods. The electrode cap distance (d_{cap}) can be controlled through the electrodeposition parameters (*e.g.* deposition time, temperature, applied potential).[(Cerquido et al., 2018)]

Due to the azimuthal symmetry of the ring-disk configuration, the electrochemical characterization in Section 3.1 is performed using a 2D axisymmetric geometry. For the simulations with virus particles presented in Section 3.2, a 2D cross-sectional geometry is employed. This is because of discrepancies in the electric field at the axis of symmetry when using an axisymmetric geometry, which causes incorrect particle behavior. Note that the current for the ring-disk configuration in Section 3.2 is still computed by integrating over a revolved geometry to ensure correct current values. For the IDE, a 2D cross-sectional geometry is used with an out-of-plane thickness of 0.5 mm. The IDE is 1 mm in length and is comprised of nearly 250 digits. Each electrode digit has a width $w_e = 2$ μm with 2 μm spacing between adjacent digits (a). The height of the microfluidic channel above the IDE is set to 15 μm and 1.07 mm in length in the simulations. Additional details pertaining to the model geometry can be found in Section S.1 of the Supplementary Information.

2.2. Electrochemical simulations

Finite element analysis is performed using COMSOL Multiphysics versions 5.5 and 5.6 with the Electrochemistry module. The Tertiary Current Distribution physics node is used. An electroneutrality condition is maintained throughout the electrolyte (*i.e.* $\sum_i z_i c_i = 0$, where z_i and c_i are the charge number and concentration of species i). As a result, the concentration of Cl^- in the KCl electrolyte is determined by the solver such that this condition is upheld. The K^+ concentration in the supporting electrolyte is made up of the KCl concentration, along with contributions from the $[Fe(CN)_6]^{4-}$. Electrochemical analysis is carried out in a generator-collector configuration whereby the two working electrodes are biased independently. For all measurements in Section 3.1, the collector is held at a bias $E_{coll} = -0.15$ V while the generator (E_{gen}) is swept across a range of potentials, except when studying the effect of collector bias where other values of E_{coll} are used (see Fig. S4). The amplification factor (Γ) and collector efficiency (η) are calculated at the end of the voltammetric sweep, where $E_{gen} = 0.6$ V. For the

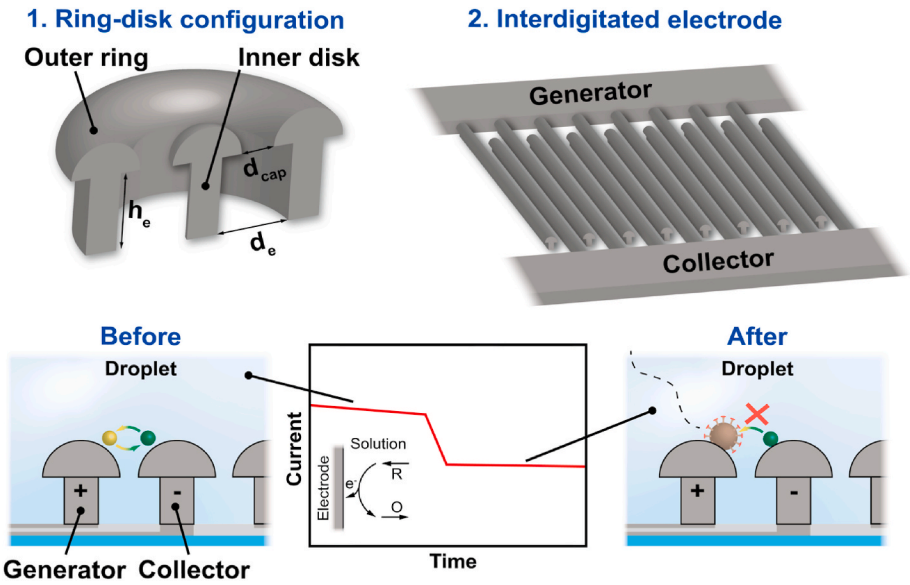

Fig. 1. A schematic representation of the ring disk (cross-section) and IDE sensor geometries along with the current quenching sensing mechanism before and after virus attachment demonstrated in this work. When a virus particle attaches, it blocks the mass transfer that drives the redox cycling. As a result, the magnitude of the electrochemical current is reduced. An example oxidation reaction is included in the inset. The reduced species (R) travels from the bulk solution to the electrode surface where it transfers an electron (e^-) to form the oxidized species (O), which then travels back to the bulk solution.

chronoamperometric measurements of Section 3.2, $E_{coll} = -0.15$ V and $E_{gen} = 0.6$ V are used. All simulations are referenced to an Ag/AgCl reference electrode ($E_{re} = 0.197$ V). The electrolyte potential (φ_l) is set equal to E_{re} at points at the top-center of the droplet ($x = 0$), or at the top of the microchannel in the IDE configuration ($x = 0$). See Fig. S1 for more details.

The mass transport of species i is governed by the Nernst-Planck equation for diffusive and migrative transport,

$$J_i = -D_i \nabla c_i - u_{m,i} z_i c_i F \nabla \varphi_l \tag{1}$$

where J_i is the flux, D is the diffusion coefficient, u_m is the mobility, F is Faraday's constant, and φ_l is the electrolyte potential. The mobility u_m of species i is related to the diffusion coefficient through the Nernst-Einstein relationship,

$$u_{m,i} = \frac{D_i}{RT} \tag{2}$$

where R is the molar gas constant, and T is the temperature. The one-electron electrochemical reaction at the electrode-electrolyte interface can be written as follows,

$$\left[Fe(CN)_6\right]^{3-} + e^- \leftrightarrow \left[Fe(CN)_6\right]^{4-} \tag{3}$$

which has a formal potential $E^0 = 0.173$ V *vs.* Ag/AgCl.[(Rock, 1966)] The resulting electrochemical current from this reaction is modeled using Butler-Volmer kinetics,

$$i = i_0 \left[\exp\left(\frac{\alpha_a nF\eta}{RT}\right) - \exp\left(-\frac{(1-\alpha_a)nF\eta}{RT}\right)\right] \tag{4}$$

where i_0 is the exchange current (dependent upon k^0, the heterogeneous rate constant), α_a is the anodic transfer coefficient, n is the number of electrons transferred in the reaction, and η is the overpotential. The overpotential is expressed as,

$$\eta = \varphi_s - \varphi_l - E_{eq} \tag{5}$$

where φ_s is the potential on the electrode boundary, φ_l is the potential in the electrolyte domain, and E_{eq} is the equilibrium potential of the redox reaction as determined by the Nernst equation,

$$E_{eq} = E^0 - \frac{RT}{nF}\log\left(\frac{c_{red}}{c_{ox}}\right) \tag{6}$$

where c_{ox} and c_{red} represent the concentration of oxidized and reduced species, respectively. The values of electrochemical parameters used are presented in Table 1.

Joule heating and heat transfer effects are coupled to the other physics modules through the Heat Transfer in Fluids physics module. The heat generated by current flow through the electrolyte is dissipated through the electrode and bottom substrate boundaries. A heat transfer coefficient (h) of 10 W m^{-2} K^{-1} is used.[(Erickson et al., 2003)] An external temperature (T_{ext}) of 298 K is used. The remaining boundaries are assumed to be insulating.

2.3. Modeling virus particles in an electric field

The virus particles are subject to a random release at $t = 0$ as the simulation begins. Each virus particle experiences drag (F_D), electrophoretic (F_{EP}), and dielectrophoretic (F_{DEP}) forces. The Stokes drag force equation can be expressed as,

$$F_D = 6\mu\pi r_p(\vec{u} - \vec{v}) \tag{7}$$

where μ is the fluid viscosity, r_p is the particle radius, $\vec{u}$ is the fluid velocity, and $\vec{v}$ is the particle velocity. For the electrolyte solution in the droplet configuration, a 30% wt. water-glycerol mixture is used to limit evaporation during practical experiments. In this case, a viscosity of 2.13×10^{-3} Pa s is calculated based on the formulation presented in ref. [(Cheng, 2008)] The density of the solution is 1.07 g cm^{-3}, [(Takamura et al., 2012)] and the dielectric constant used is 68.[(Åkerlöf, 1932)] The virus particle density is 1.3 g cm^{-3}, which is similar to previous reports.[(Ermolina et al., 2006)] For IDE design, which is embedded in a microfluidic channel, simulations are done in an aqueous KCl electrolyte without added glycerol. The enclosed nature of the microfluidic channel eliminates the need for the use of glycerol.

The electrophoretic force on a particle is given as,

$$F_{EP} = -eq\nabla\varphi_l \tag{8}$$

where e is the elementary charge, q is the charge number of the particle, and φ_l is again the electrolyte potential, which is obtained by coupling with the Electrochemistry module. The dielectrophoretic force can be written as,

$$F_{DEP} = 2\pi r_p^3 \varepsilon_0 Re(\varepsilon_m) Re(K) \nabla \left|\vec{E}\right|^2 \tag{9}$$

Table 1
The electrochemical parameters used in simulations [(Ma et al., 2013; Konopka and McDuffie, 1970)].

Parameter	Value
$c_{red}{}^*$	1 mM
k^0	0.1 cm s^{-1}
D_{ox}	7.2×10^{-6} cm^2 s^{-1}
D_{red}	6.4×10^{-6} cm^2 s^{-1}
α_a	0.50
n	1

where ε_0 is the permittivity of free space, ε_m is the dielectric constant of the medium, K is the Clausius-Mossotti function ($K = \frac{\varepsilon_p{}^* - \varepsilon_m{}^*}{\varepsilon_p{}^* + 2\varepsilon_m{}^*}$ where ε_p is the dielectric constant of the particle), and $\vec{E}$ is the electric field. The asterisk denotes the complex dielectric constant given as $\varepsilon_r{}^* = \varepsilon_r - j\sigma/\omega$ where j, σ, and ω represent the imaginary unit, electrical conductivity, and angular frequency, respectively. The dielectric constant of the droplet solution (glycerol-water mixture) is 68, whereas the dielectric constant for the aqueous electrolyte in the IDE microchannel is obtained from the COMSOL material library.

The virus particles are modeled as an inner sphere with an encapsulating outer layer with dielectric constants of $\varepsilon_1 = 75$ and $\varepsilon_2 = 7.5$, respectively, unless otherwise noted.[(Hughes et al., 2002)] The effective dielectric constant of a sphere with an outer shell can be calculated with Eq. (10),

$$\varepsilon_{p,eff} = \varepsilon_2{}^* \frac{\left(r_2/r_1\right)^3 + 2\frac{\varepsilon_1{}^* - \varepsilon_2{}^*}{\varepsilon_1{}^* + 2\varepsilon_2{}^*}}{\left(r_2/r_1\right)^3 - \frac{\varepsilon_1{}^* - \varepsilon_2{}^*}{\varepsilon_1{}^* + 2\varepsilon_2{}^*}} \tag{10}$$

where r_2 is the total particle radius from center to outer shell, r_2 is the radius of just the inner sphere, and ε_1 and ε_2 are the dielectric constants of the shell and core, respectively.

3. Results & discussion

3.1. Electrochemical analysis of the ring-disk (droplet) configuration

Before introducing the virus particles into the models, the baseline electrochemical properties are evaluated in the absence of virus particles. The disk and ring microelectrodes are located at the center of a 1 μl hemispherical droplet containing 1 mM $[Fe(CN)_6]^{4-}$ ($E^0 = 0.173$ V *vs.* Ag/AgCl) in a supporting KCl electrolyte (1 mM) (see Fig. S2 for the effect of $[Fe(CN)_6]^{4-}$ concentration). At the top, both electrodes have a mushroom-like cap that can be created *via* a template-driven overgrowth during electrodeposition, similar to reports from Garimella et al.[(Chen et al., 2015; Chandramohan et al., 2016)] An advantage of this overgrowth is that the spacing between generator and collector electrode caps (d_{cap}) is tunable and can be decreased beyond the predefined pillar spacing by controlling the electrodeposition current and duration.[(Cerquido et al., 2018)] Decreasing the generator-collector spacing is crucial for the diffusion-driven redox cycling process, [(Zafarani et al., 2016)] while the high aspect ratio of the three-dimensional electrodes enables better confinement of redox species [(Morita et al., 2014; Odijk et al., 2008)] and results in an increased amplification factor ($\Gamma \equiv I_{dual-mode}/I_{single-mode}$), [(Zafarani et al., 2016)] where $I_{dual-mode}$ and $I_{single-mode}$ represent the steady-state current with and without redox cycling, respectively.

Fig. 2a demonstrates the enhancement of the dual-mode Faradaic current, resulting from the recycling of redox-active species, compared to single electrode-mode. The linear sweep voltammograms (LSV) in Fig. 2a are carried out at a scan rate of 50 mV s^{-1} (see Fig. S3 for effect of scan rate) with E_{gen} ranging from −0.2 to 0.6 V while E_{coll} is either held constant at −0.15 V in dual-mode (see Fig. S4 for effect of different generator biases) or left floating in single-mode. The current shows the typical steady-state behavior encountered with microelectrodes. The subsequent concentration profiles for the oxidized species (c_{ox}) are shown in Fig. 2b and c at four points during the potential scan. As expected in the dual-mode configuration, a steep concentration gradient forming at $E_{gen} = 0.2$ V is seen between generator and collector electrodes that is not seen in single-mode. Because the flux of a species at an electrode is dependent on the concentration gradient, redox cycling can result in substantial amplification factors and explains the increased generator current seen in Fig. 2a.

Typically, in electrochemical experiments, a sufficiently conductive electrolyte is used to minimize the ohmic drop in solution. Fig. S5 demonstrates the effect of KCl electrolyte concentration on the voltammetric current. As the KCl concentration increases, the steady-state current magnitude slightly decreases. This may be due to less migrative transport of the charged redox probe as electrolyte concentration increases. As a result, at lower KCl concentration, a larger portion of the current carrying ions will be $[Fe(CN)_6]^{3-/4-}$ rather than K^+ and Cl^-. The lower electrolyte concentration also supports a larger electric field, which will be advantageous for electrophoretic transport of the virus particles discussed later. Moreover, because Joule heating of the electrolyte scales with conductivity σ_m ($Q \propto \sigma_m$, where Q represents the heat generated), [(Cornejo and Linz, 2021; Yan et al., 2008)] it is advantageous to use a lower conductivity electrolyte to minimize these effects. Fig. S6 shows the temperature in the electrolyte after a 1200 s amperometric scan. Only minor temperature differences of a few mK are seen in the immediate region surrounding the electrode, which are not likely to cause any significant degradation in operational performance.

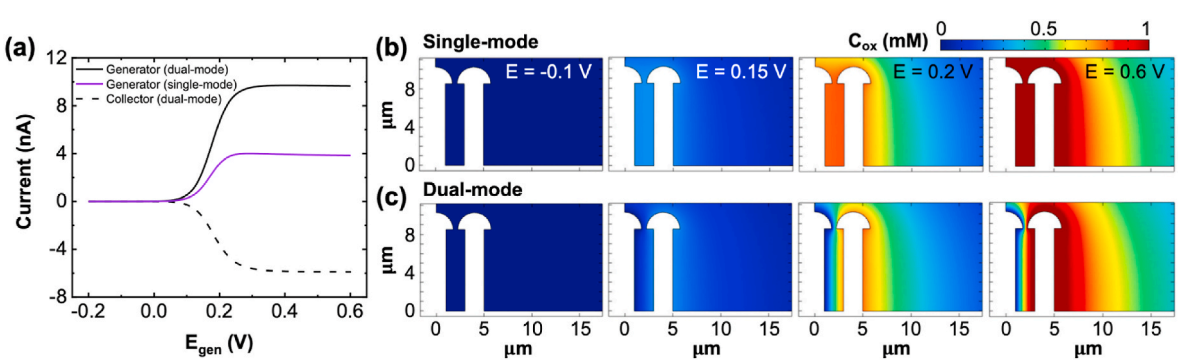

Fig. 2. **a)** A representative voltammogram of the ring-disk microelectrode configuration in single- and dual-mode (1 mM $[Fe(CN)_6]^{4-}$, 1 mM KCl, scan rate = 50 mV s^{-1}, $E_{coll} = -0.15$ V or floating). The resulting concentration profiles of $[Fe(CN)_6]^{3-}$ are shown for **b)** single-mode, and **c)** dual-mode over the course of the voltammetric scan. Note that the formal potential of the redox probe is around 0.17 V.

Fig. 3 highlights the effect of electrode geometry, which plays an important role in determining the redox cycling capabilities.[(Wolfrum et al., 2016; Ma et al., 2013; Zafarani et al., 2016; Xiong et al., 2015)] In particular, the impact of cap spacing (d_{cap}, left column of Fig. 3), electrode height (h_e, middle column of Fig. 3), and electrode spacing (d_e, right column of Fig. 3) are evaluated. Regarding the cap spacing, the amplification factor Γ ranges from ~4.2 at d_{cap} = 0.05 μm down to ~2.05 for d_{cap} = 1.8 μm, the largest spacing studied. Likewise, the collector efficiency ($\eta \equiv I_{coll}/I_{gen}$) follows a similar trend, ranging from 0.78 for d_{cap} = 0.05 μm down to 0.55 for d_{cap} = 1.8 μm. Although a smaller d_{cap} leads to improved redox cycling behavior, decreasing d_{cap} beyond a few 100 nm could be difficult to control during the overgrowth electrodeposition. To improve process robustness and consistency, spacings of 0.1 μm and above may be more suitable for experimental realization of the proposed system from a technical standpoint.

More substantial differences in η and Γ are seen when varying the electrode spacing d_e. For d_e = 20 μm, Γ is less than 1.2 and η ~0.13, whereas decreasing d_e to 0.6 μm increases Γ nearly four-fold to ~4.8 and η to ~0.8. Interestingly, around d_e = 8 μm and larger, the cycling between collector and generator is minimized due to decreased overlap in diffusion layers (see Fig. S7). This is evident by the onset of an oxidation peak in the LSV data seen at 8 μm, and especially at 15 and 20 μm, as opposed to the steady-state sigmoidal behavior typically seen with microelectrodes.[(Xiong et al., 2015)] This points to mass transfer limitations similar to those seen with macroelectrodes. The onset of an oxidation peak can also be seen in the single-mode configurations presented in Fig. S8, thus signifying the importance of redox cycling in maintaining steady-state conditions and minimizing depletion of the redox species. To ensure adequate amplification and collection is upheld, an electrode spacing of 2 μm or less is recommended.

The electrode height (h_e) does have implications on η and Γ, albeit much less of an impact than d_e. Across the range of h_e from 1 to 10 μm studied in this work, Γ only varies from ~2.1 to 2.6 with the collector efficiency following a similar trend. However, this may be advantageous as increasing the height beyond 10 μm could present fabrication challenges associated with the photoresist thickness (*i.e.* electrodeposition mold layer). With the above factors taken into consideration, in addition to potential challenges that could occur during the device fabrication process, a generator-collector electrode spacing of d_e = 2 μm, electrode height of h_e = 8.5 μm, and cap spacing of d_{cap} = 0.5 μm is used for subsequent simulations.

3.2. Electrochemical analysis in the presence of virus particles (droplet configuration)

After evaluating the electrochemical properties of the microelectrodes, we introduce virus particles into the simulation to better understand the detection capability of the proposed system. The virus

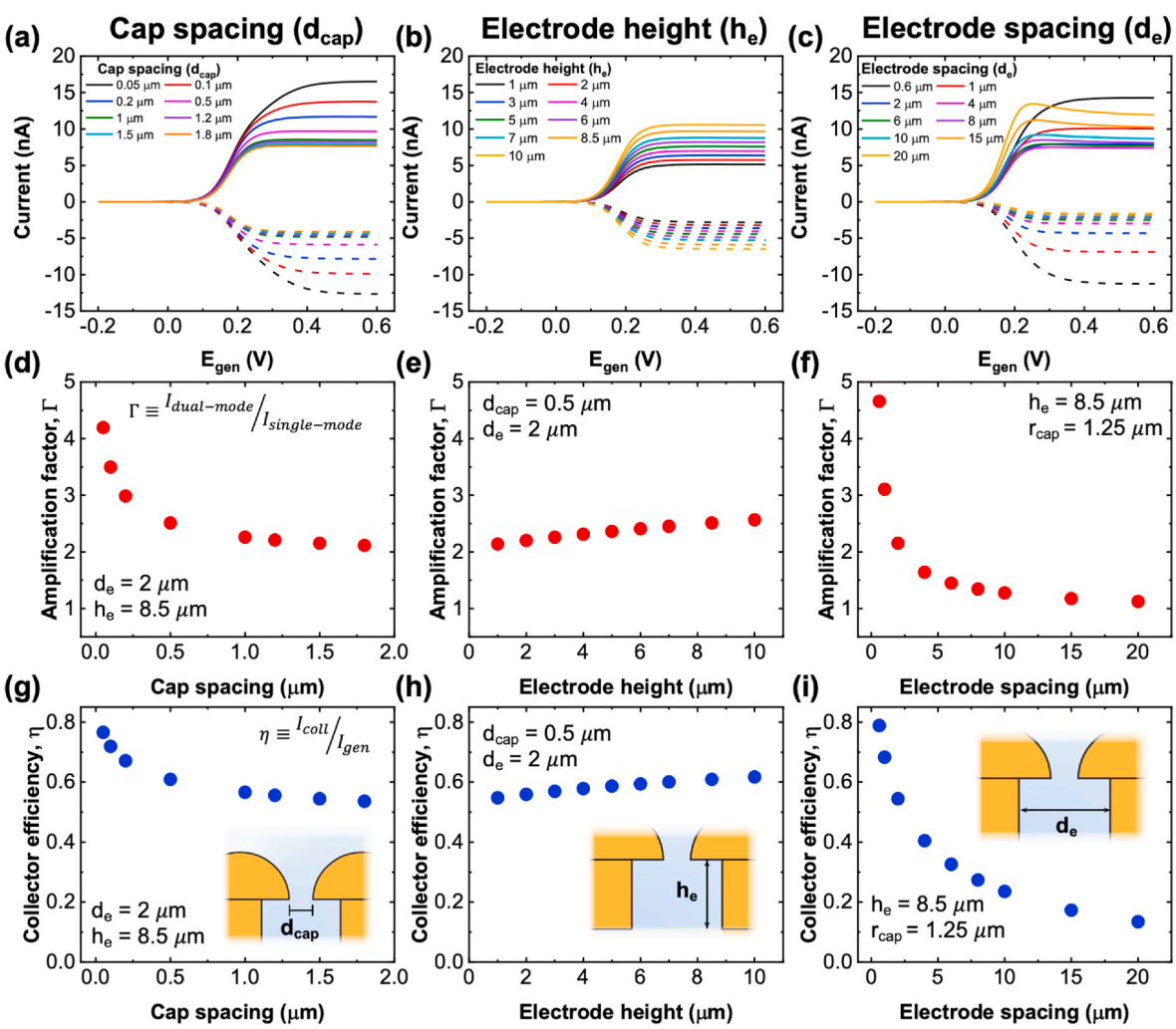

Fig. 3. The effect of generator-collector geometry on the redox cycling characteristics. **a-c)** The linear sweep voltammograms (*Parameters*: 1 mM $[Fe(CN)_6]^{4-}$, 1 mM KCl, scan rate = 50 mV s^{-1}, E_{coll} = −0.15 V) demonstrating the effect of cap spacing (d_{cap}), electrode height (h_e), and electrode spacing (d_e), respectively. **d-f)** The subsequent amplification factors (Γ) and **g-i)** collector efficiencies (η) as functions of electrode geometry.

particles are modeled as spherical core-shell structure, each layer having unique dielectric properties.[(Hughes et al., 2002; MacCuspie et al., 2008)] Typically, the outer shell has a dielectric constant on the order of $\varepsilon_2 = 5$–10 while the ε_1 is around 70–80.[(Hughes et al., 1998; Morgan et al., 1999; Yan and Wu, 2008)] Of particular interest for electrophoretic transport are the virus charge (q), virus count (N), and virus size (d_p). Some reports have estimated the net surface charge of different viruses, such as Cowpea Mosaic Virus (CPMV), which is estimated to have a charge of (negative) 200e (where e is the elementary unit of charge) per virion (or 0.013 C m^{-2}).[(Ermolina et al., 2006)] Similarly, for Cowpea Chlorotic Mottle Virus (CCMV), a surface charge of (negative) 150e - 200e is estimated based on electrophoretic mobility (μ_{EP}) data at neutral pH.[(Vega-Acosta et al., 2014)] For Tobacco Mosaic Virus (TMV) the surface charge density is even higher, at 0.043 C m^{-2}[(Ermolina et al., 2003)] The charged nature of the virus particles serves as the basis for electrophoretic enrichment as demonstrated here.

We simulate the chronoamperometric response (see Figs. S9–S11 for unprocessed amperometric data) with four different particle charges – 0, −100, −200, and −300 (in units of e) – and three particle sizes – 30, 120, and 200 nm – to better understand how the charge and size of a particle impacts the sensor response, specifically particle capture time and number of capture events. The chronoamperometric simulations are performed in dual-mode configuration with $E_{coll} = -0.15$ V and $E_{gen} = 0.6$ V, which significantly reduces the virus capture time (from ~740 s down to ~20 s), due to a stronger electric field, and results in larger current steps (~0.265 pA *vs.* 0.013 pA), due to the larger amplified current compared to single-mode (see Fig. S12 for results of simulations done in single-mode). As shown in Fig. 4a, in the absence of any surface charge ($q = 0$), no virus particles attach to the electrode. As the charge increases, the electrophoretic force (F_{EP}) increases proportionally, resulting in more capture events (2 for $q = -300$ opposed to 1 for other charge values) and reduced capture time. The current steps shown in Fig. 4 are proportional to the surface area of the virus particle ($I_{step} \propto r_p^2$)[(Bonezzi and Boika, 2017)] and result in a ~1 pA current step for a 70 nm particle, which is similar in magnitude to previously reported values using murine cytomegalovirus.[(Dick et al., 2016)] More pronounced steps in current are seen for larger particles, shown in Fig. 4b. It is worth noting that viruses such as SARS-CoV and SARS-CoV-2 have been reported to be on the order of 70–100 nm, [(Goldsmith et al., 2004; Menter et al., 2020)] with reports ranging from around 50 nm for SARS-CoV [(Shieh et al., 2005)] up to 140 nm for SARS-CoV-2.[(Zhu et al., 2020)] Other viruses, such as herpes simplex virus, can be 250 nm in size [(Hughes et al., 2002)] while hepatitis A virus particles have been reported to be just 27 nm in size.[(Grom et al., 2006)] Sepunaru et al. demonstrated single-particle capture events of influenza virus (measured size ~ 125 nm) conjugated with silver nanoparticles.[(Sepunaru et al., 2016)] They showed current spikes on the order of 10 pA due to oxidation of the nanoparticles upon capture at the electrode. In our case, for a particle size of 200 nm, we see step sizes of ~5 pA, which is comparable to previous reports using silica nanoparticles. [(Boika et al., 2012)]

Interestingly, the time required for the first capture event increases with particle size, likely a result of the larger drag force (F_D). Although particle size has implications in both the drag force ($F_D \propto d_p$) and dielectrophoretic force ($F_{DEP} \propto d_p^3$) acting on the particle, for DC measurements such as those here, we find F_{DEP} does not contribute significantly to the transport of the virus particles (see Fig. S13 for a comparison of average forces acting on the virus particles). Increasing the number of particles results in more capture events as shown in Fig. 4c, although no response is seen for $N = 1$, there is only one capture event for $N = 5$.

In an effort to improve the number of capture events and achieve the ultimate goal of single-entity detection, we confine the droplet volume from 1 μl down to 2 nl. Droplets of this scale and even smaller can be created and manipulated using a microcapillary pressure injection system.[(Salm et al., 2013)] Alternatively, controlled evaporation of the droplet has been utilized as a pre-concentration strategy as well.[(Ebrahimi et al., 2013)] Nanoliter volumes are also commonly achieved in microfluidic channels which will be discussed in regard to the IDE structure in Section 3.3. Fig. 5a shows the amperometric current for $N = 2$ for a particle size of $d_p = 70$ nm in a 2 nl droplet. With 2 virus particles present, one particle is sufficiently far away such that it is not attracted to the electrode over the time frame tested. The other particle can be seen attaching after ~40 min. The corresponding time evolution of the virus capture is shown in Fig. 5b with the electric field.

One possible drawback of performing electrochemical measurements in such confined geometries on the timescales shown here is the extent of the diffusion layer. Estimating the diffusion layer as $l \sim (Dt)^{1/2}$, one obtains a layer of roughly 1 mm, well beyond the confines of the droplet. In the absence of redox cycling, the analyte supply is depleted after about 60 s, and the current diminishes to ~0 (see Fig. S14). However, our configuration takes advantage of redox cycling to constantly resupply $[Fe(CN)_6]^{3-/4-}$, leading to a finite steady-state current and allowing for virus detection to continue within the droplet. Due to these constraints associated with the droplet geometry, the amperometric current of the 2 nl droplet is slightly less than the 1 μl droplet (see Fig. S15).

3.3. Electrochemical analysis in the presence of virus particles (IDE configuration)

After demonstrating the virus capture ability of an isolated generator-collector ring-disk pair in a droplet configuration, we investigate an interdigitated electrode (IDE) design, which is more suitable for integration with microfluidic channels rather than individual droplets. As discussed below, the IDE also improves detection at lower particle number, which may be an issue with the droplet configuration. The

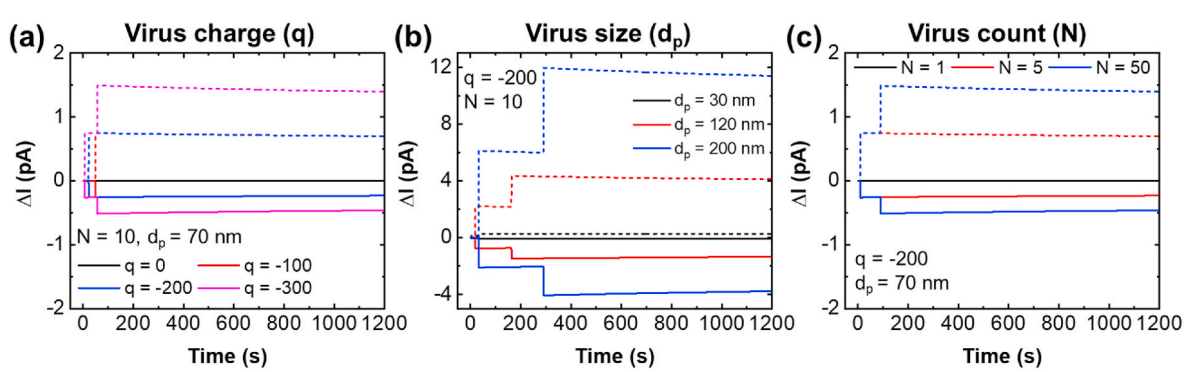

Fig. 4. The effect of various virus properties on the amperometric detection of capture events in a 1 μl droplet. **a)** The background subtracted current (ΔI) obtained from chronoamperometric measurements demonstrating the effect of the virus surface charge (q), **b)** The effect of virus size (d_p), and **c)** The effect of virus number (N). The solid and dashed lines represent the generator and collector current, respectively. *Parameters*: 1 mM $[Fe(CN)_6]^{4-}$, 1 mM KCl, $E_{coll} = -0.15$ V, $E_{gen} = 0.6$ V.

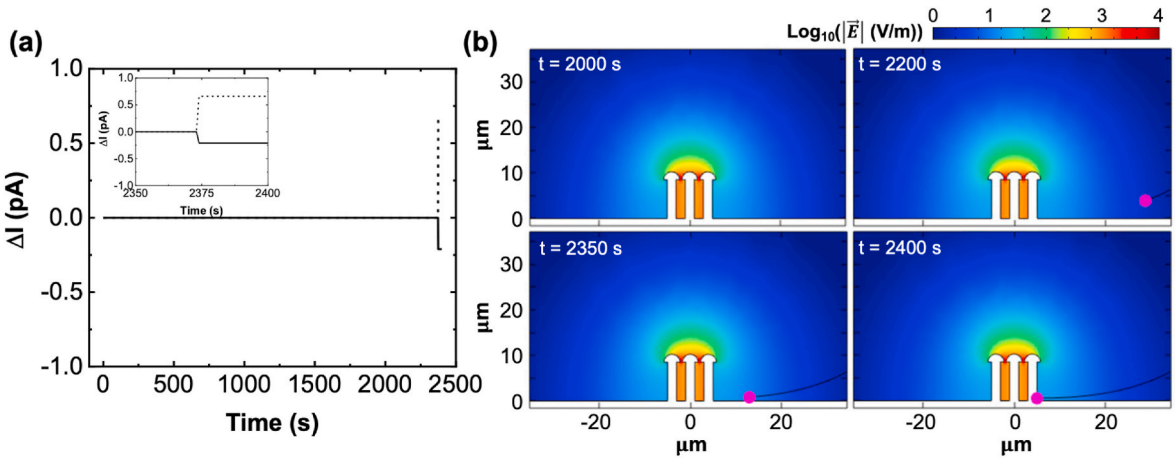

Fig. 5. **a)** The background subtracted current (ΔI) obtained from chronoamperometric measurements within a 2 nl droplet demonstrating the current steps caused by virus particle attachment to the electrode surface for $N = 2$. Solid and dashed lines represent the generator and collector currents, respectively. Inset shows a close up image of the capture event near 2375 s. **b)** The electric field at a sampling of time points showing the evolution of the particle attachment to the electrode surface. *Parameters*: 1 mM $[Fe(CN)_6]^{4-}$, 1 mM KCl, $E_{coll} = -0.15$ V, $E_{gen} = 0.6$ V, $d_p = 70$ nm, $q = -200$.

IDE structure is a common generator-collector configuration whereby sub-micrometer spacing (a) is traditionally achieved using more costly fabrication methods, such as electron beam lithography.[(Wolfrum et al., 2016)] The proposed template-driven overgrowth method is also applicable here and can be used to further reduce the lateral spacing between generator and collector. In our analysis, the IDE with overgrown cap is placed within a microfluidic channel of 15 μm in height, which inherently confines the virus particles close to the electrodes. Fig. 6a shows the electric field distribution of an exemplary cross section of the IDE with electrode spacing $d_e = 2$ μm, $h_e = 2$ μm, and $d_{cap} = 0.5$ μm. Again, $E_{coll} = -0.15$ V and $c_{KCl} = 1$ mM (see Figs. S16 and S17 for effect of collector bias and KCl concentration). Electric fields above 1 kV m^{-1} in magnitude are seen in the immediate vicinity of the electrode, which is sufficient for electrophoretic manipulation. Fig. 6b highlights the concentration profile of $[Fe(CN)_6]^{4-}$ at the generator and collector. Significant overlap in the diffusion layers of adjacent electrodes is apparent, which allows the IDE to reach a steady-state current during the LSV scan that is not seen in single-mode. In fact, without redox cycling, the $[Fe(CN)_6]^{4-}$ is depleted very rapidly during LSV, resulting in the current dropping to near 0 before the scan is complete (see Figs. S18 and S19).

The IDE structure is evaluated with $N = 1$ and 2 virus particles of 70 nm size and $q = -200$, similar to our previous studies with the droplet configuration (Section 3.2). The background subtracted current for both $N = 1$ and 2 is presented in Fig. 6c (the unprocessed chronoamperometry data are shown in Fig. S20). The particle attaches very quickly in the IDE configuration – after just 1 s. This is a significant improvement over the isolated generator-collector ring-disk geometry, which only recorded one capture event with $N = 2$ and no capture events with $N = 1$ in the 2 nl droplet. The main drawback of using such a large area electrode is the reduced blocking effect caused by the attachment of the virus particle compared with the much smaller ring-disk geometry. As a result, the relative reduction in current per virus particle attachment is smaller.

The proposed biosensor scheme has the potential to enable rapid and sensitive electrochemical "particle counting" with low fabrication costs. While the focus of this study was to demonstrate detection time and sensitivity, it can be complemented by other methods to enable selective detection as well. This can be achieved by incorporating biorecognition elements specific to the virus of interest. One example from Dick et al. used glucose oxidase (GOx)-modified antibodies that attached to the surface of the target virus.[(Dick et al., 2016)] As the virus-antibody-GOx unit adsorbed on the electrode surface, the GOx acted as a reducing agent for the $FcMeOH^+$ being generated at the electrode surface, which allowed for re-oxidation of the FcMeOH and significant amplification of the signal. An alternative approach could be to extract the target virus from the sample matrix using magnetic nanoparticles (MNPs) conjugated with the corresponding antibody or aptamer. The virus-MNP conjugate can then be selectively resuspended in the test solution for downstream counting. If needed, by using a thermally reversible conjugation mechanism, such as the Diels-Alder approach (Gregoritza and Brandl, 2015), the virus particles could be removed from the MNPs *via* heating.

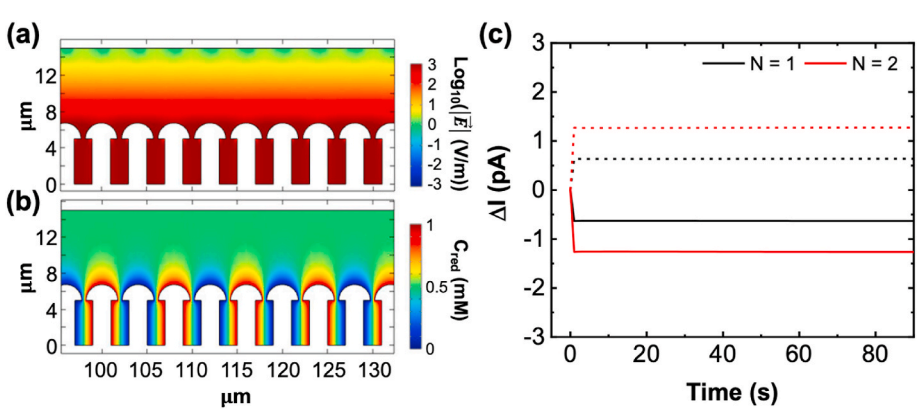

Fig. 6. **a)** The electric field distribution of a cross section sample of the interdigitated electrode (IDE) and microchannel. **b)** The concentration profile of c_{red} showing the overlapping diffusion layers of adjacent generator and collector electrodes. **c)** The background subtracted current (ΔI) obtained from chronoamperometric measurements demonstrating the current steps caused by virus particle attachment to the electrode surface. Note that the attachment occurs within 1 s for both $N = 1$ and $N = 2$. Solid and dashed lines represent the generator and collector currents, respectively. *Parameters*: 1 mM $[Fe(CN)_6]^{4-}$, 1 mM KCl, $E_{coll} = -0.15$ V, $E_{gen} = 0.6$ V, $d_p = 70$ nm, $q = -200$.

4. Conclusion

In this work, we propose a novel biosensor concept for single virus counting using two tunable generator-electrode configurations. The proposed design combines redox cycling with electrophoresis-driven electrode-particle collision for rapid and sensitive virus detection. The impact of various experimental and geometric parameters on the electrochemical signal is investigated using detailed finite element analysis. These designs (either droplet-based or channel-based designs) have the potential for integration with microfluidic and other lab-on-a-chip platforms for portable, point-of-care virus detection. Amplification factors and collector efficiencies are highly dependent on the generator-collector spacing and range from beyond 4 to as little as ~1.1 for the amplification factor and from 0.8 down to less than 0.2 for the collector efficiency. While the redox amplification reported here is modest compared to previous reports which often use nanofabrication methods, we should emphasize that the dimensions of the proposed device is well within the capabilities of standard photolithography techniques. Moreover, the overgrowth strategy is compatible with scalable electrodeposition methods. Strategies to improve the amplification, such as nanocavity-based sensors, could be employed, but may limit the reach of the electric field into the bulk solution and make the electrophoretic enrichment of viral particles challenging.

The detection scheme detailed in this report relies on the virus particle blocking the mass transfer of the electrochemical redox probe upon colliding with the electrode, which causes a detectable step in the amperometric current. The nature of the collisions is found to depend on the virus surface charge, size, and quantity. Although the ring-disk design (droplet configuration) is more sensitive to virus attachment due to smaller surface area, the IDE design (microchannel configuration) takes advantage of a large capture area and particle confinement within the microchannel to detect virus particles on the order of seconds. The present FEA results provide valuable guidance for the practical fabrication of biosensors suitable for single particle counting, which has potentially broad applications ranging from electrochemical virus detection to immunoassays and molecular diagnostics.

Finally, while this work focused on establishing general design rules for sensing based on redox cycling and electrophoretic particle enrichment, future computational investigations into how the location of particle attachment impacts the measured current step size would be beneficial. Such studies would shed light on how particles of the same size can result in different current step magnitudes due to inhomogeneous flux of electroactive species across the electrode surface, therefore better quantifying the range of step sizes to be expected experimentally.

CRediT authorship contribution statement

Derrick Butler: Conceptualization, Methodology, Investigation, Visualization, Writing – original draft, preparation, Writing – review & editing. **Aida Ebrahimi:** Conceptualization, Methodology, Supervision, Visualization, Funding acquisition, Writing – review & editing.

Declaration of competing interest

The authors declare that they have no known competing financial interests or personal relationships that could have appeared to influence the work reported in this paper.

Acknowledgments

The authors would like to acknowledge the Roar supercomputing resources of the Penn State Institute for Computational and Data Sciences (ICDS). Research reported in this manuscript is partially supported by the National Institutes of Health (award numbers R21EB031354 and R21GM132793). The content is solely the responsibility of the authors and does not necessarily represent the official views of the National Institutes of Health.

Appendix A. Supplementary data

Supplementary data to this article can be found online at https://doi.org/10.1016/j.bios.2022.114198.

References

Åkerlöf, G., 1932. Dielectric constants of some organic solvent-water mixtures at various temperature. J. Am. Chem. Soc. 54, 4125–4139.
Arai, H., Petchclai, B., Khupulsup, K., Kurimura, T., Takeda, K., 1999. Evaluation of a rapid immunochromatographic test for detection of antibodies to human immunodeficiency virus. J. Clin. Microbiol. 37, 367–370.
Baig, A.M., 2021. Chronic COVID Syndrome: need for an appropriate medical terminology for long-COVID and COVID long-haulers. J. Med. Virol. 93, 2555–2556.
Bard, A.J., Faulkner, L.R., 2001. Electrochemical Methods: Fundamentals and Applications, second ed. John Wiley and Sons, Inc, New York.
Ben-Yoav, H., Winkler, T.E., Kim, E., Chocron, S.E., Kelly, D.L., Payne, G.F., Ghodssi, R., 2014. Redox cycling-based amplifying electrochemical sensor for in situ clozapine antipsychotic treatment monitoring. Electrochim. Acta 130, 497–503.
Boika, A., Thorgaard, S.N., Bard, A.J., 2012. Monitoring the electrophoretic migration and adsorption of single insulating nanoparticles at ultramicroelectrodes. J. Phys. Chem. B 117, 4371–4380.
Bonezzi, J., Boika, A., 2017. Deciphering the magnitude of current steps in electrochemical blocking collision experiments and its implications. Electrochim. Acta 236, 252–259.
Bustin, S.A., 2000. Absolute quantification of mrna using real-time reverse transcription polymerase chain reaction assays. J. Mol. Endocrinol. 25, 169–193.
Caygill, R.L., Blair, G.E., Millner, P.A., 2010. A review on viral biosensors to detect human pathogens. Anal. Chim. Acta 681, 8–15.
Cerquido, M., Proenca, M.P., Dias, C., Leitao, D.C., Cardoso, S., Freitas, P.P., Aguiar, P., Ventura, J., 2018. Tailoring the cap's morphology of electrodeposited gold micro-mushrooms. Appl. Surf. Sci. 445, 512–518.
Chandramohan, A., Dash, S., Weibel, J.A., Chen, X., Garimella, S.V., 2016. Marangoni convection in evaporating organic liquid droplets on a nonwetting substrate. Langmuir 32, 4729–4735.
Chen, X., Weibel, J.A., Garimella, S.V., 2015. Water and ethanol droplet wetting transition during evaporation on omniphobic surfaces. Sci. Rep. 5, 17110.
Cheng, N.-S., 2008. Formula for the viscosity of a glycerol-water mixture. Ind. Eng. Chem. Res. 47, 3285–3288.
Clegg, A.D., Rees, N.V., Banks, C.E., Compton, R.G., Clegg,] A D, Banks, C.E., Compton, R.G., Rees, N.V., 2006. Ultrafast chronoamperometry of single impact events in acoustically agitated solid particulate suspensions. ChemPhysChem 7, 807–811.
Cornejo, M.A., Linz, T.H., 2021. Harnessing Joule heating in microfluidic thermal gel electrophoresis to create reversible barriers for cell enrichment. Electrophoresis 42, 1238–1246.
Dick, J.E., 2016. Electrochemical detection of single cancer and healthy cell collisions on a microelectrode. Chem. Commun. 52, 10906–10909.
Dick, J.E., Hilterbrand, A.T., Strawsine, L.M., Upton, J.W., Bard, A.J., 2016. Enzymatically enhanced collisions on ultramicroelectrodes for specific and rapid detection of individual viruses. Proc. Natl. Acad. Sci. U.S.A. 113, 6403–6408.
Ebrahimi, A., Dak, P., Salm, E., Dash, S., Garimella, S.V., Bashir, R., Alam, M.A., 2013. Nanotextured superhydrophobic electrodes enable detection of attomolar-scale DNA concentration within a droplet by non-faradaic impedance spectroscopy. Lab Chip 13, 4248–4256.
Erickson, D., Sinton, D., Li, D., 2003. Joule heating and heat transfer in poly (dimethylsiloxane) microfluidic systems. Lab Chip 3, 141–149.
Ermolina, I., Morgan, H., Green, N.G., Milner, J.J., Feldman, Y., 2003. Dielectric spectroscopy of Tobacco mosaic virus. Biochim. Biophys. Acta Gen. Subj. 1622, 57–63.
Ermolina, I., Milner, J., Morgan, H., 2006. Dielectrophoretic investigation of plant virus particles: cow pea mosaic virus and Tobacco mosaic virus. Electrophoresis 27, 3939–3948.
Fox, J.D., 2007. Respiratory virus surveillance and outbreak investigation. J. Clin. Virol. 40, S24–S30.
Frkonja-Kuczin, A., Ray, L., Zhao, Z., Konopka, M.C., Boika, A., 2018. Electrokinetic preconcentration and electrochemical detection of Escherichia coli at a microelectrode. Electrochim. Acta 280, 191–196.
Goines, S., Dick, J.E., 2020. Review—electrochemistry's potential to reach the ultimate sensitivity in measurement science. J. Electrochem. Soc. 167, 037505.
Goldsmith, C.S., Tatti, K.M., Ksiazek, T.G., Rollin, P.E., Comer, J.A., Lee, W.W., Rota, P. A., Bankamp, B., Bellini, W.J., Zaki, S.R., 2004. Ultrastructural characterization of SARS Coronavirus. Emerg. Infect. Dis. 10, 320–326.
Goluch, E.D., Wolfrum, B., Singh, P.S., Zevenbergen, M.A.G., Lemay, S.G., 2009. Redox cycling in nanofluidic channels using interdigitated electrodes. Anal. Bioanal. Chem. 394, 447–456.
Gregoritza, M., Brandl, F.P., 2015. The diels–alder reaction: a powerful tool for the design of drug delivery systems and biomaterials. Eur. J. Pharm. Biopharm. 97, 438–453.

Grom, F., Kentsch, J., Müller, T., Schnelle, T., Stelzle, M., 2006. Accumulation and trapping of hepatitis A virus particles by electrohydrodynamic flow and dielectrophoresis. Electrophoresis 27, 1386–1393.
Gross, A.J., Holmes, S., Dale, S.E.C., Smallwood, M.J., Green, S.J., Peter Winlove, C., Benjamin, N., Winyard, P.G., Marken, F., 2015. Nitrite/nitrate detection in serum based on dual-plate generator-collector currents in a microtrench. Talanta 131, 228–235.
Guo, J., Wei, T., Huang, Q., Li, M., Yang, C., Mou, J., Shi, L., Gao, T., Li, G., 2022. Direct acupuncture of nitric oxide by an electrochemical microsensor with high time-space resolution. Biosens. Bioelectron. 195, 113667.
Hellberg, D., Scholz, F., Schauer, F., Weitschies, W., 2002. Bursting and spreading of liposomes on the surface of a static mercury drop electrode. Electrochem. Commun. 4, 305–309.
Hellberg, D., Scholz, F., Schubert, F., Lovrić, M., Omanović, D., Hernández, V.A., Thede, R., 2005. Kinetics of liposome adhesion on a mercury electrode. J. Phys. Chem. B 109, 14715–14726.
Hopkins University, Johns. COVID-19 dashboard by the Center for Systems Science and Engineering (CSSE) at Johns Hopkins University (JHU). https://coronavirus.jhu.edu/map.html. Feb 22, 2022.
Hughes, M.P., Morgan, H., Rixon, F.J., Burt, J.P.H., Pethig, R., 1998. Manipulation of herpes simplex virus type 1 by dielectrophoresis. Biochim. Biophys. Acta Gen. Subj. 1425, 119–126.
Hughes, M.P., Morgan, H., Rixon, F.J., 2002. Measuring the dielectric properties of herpes simplex virus type 1 virions with dielectrophoresis. Biochim. Biophys. Acta Gen. Subj. 1571, 1–8.
Ito, M., Watanabe, M., Nakagawa, N., Ihara, T., Okuno, Y., 2006. Rapid detection and typing of influenza A and B by loop-mediated isothermal amplification: comparison with immunochromatography and virus isolation. J. Virol. Methods 135, 272–275.
Kätelhön, E., Hofmann, B., Lemay, S.G., Zevenbergen, M.A.G., Offenhäusser, A., Wolfrum, B., 2010. Nanocavity redox cycling sensors for the detection of dopamine fluctuations in microfluidic gradients. Anal. Chem. 82, 8502–8509.
Kievits, T., van Gemen, B., van Strijp, D., Schukkink, R., Dircks, M., Adriaanse, H., Malek, L., Sooknanan, R., Lens, P., 1991. NASBATM isothermal enzymatic in vitro nucleic acid amplification optimized for the diagnosis of HIV-1 infection. J. Virol. Methods 35, 273–286.
Kisely, S., Warren, N., McMahon, L., Dalais, C., Henry, I., Siskind, D., 2020. Occurrence, prevention, and management of the psychological effects of emerging virus outbreaks on healthcare workers: rapid review and meta-analysis. BMJ 369, m1642.
Konopka, S.J., McDuffie, B., 1970. Diffusion coefficients of ferri- and ferrocyanide ions in aqueous media, using twin-electrode thin-layer electrochemistry. Anal. Chem. 42, 1741–1746.
Lebègue, E., Anderson, C.M., Dick, J.E., Webb, L.J., Bard, A.J., 2015. Electrochemical detection of single phospholipid vesicle collisions at a Pt ultramicroelectrode. Langmuir 31, 11734–11739.
Lee, J.Y., Kim, B.-K., Kang, M., Park, J.H., 2016. Label-free detection of single living bacteria via electrochemical collision event. Sci. Rep. 6, 1–6, 2016 61.
Lee, G.-Y., Park, J.-H., Wook Chang, Y., Cho, S., Kang, M.-J., Pyun, J.-C., 2018. Chronoamperometry-based redox cycling for application to immunoassays. ACS Sens. 3, 106–112.
Ma, C., Contento, N.M., Gibson, L.R., Bohn, P.W., 2013. Redox cycling in nanoscale-recessed ring-disk electrode arrays for enhanced electrochemical sensitivity. ACS Nano 7, 5483–5490.
MacCuspie, R.I., Nuraje, N., Lee, S.Y., Runge, A., Matsui, H., 2008. Comparison of electrical properties of viruses studied by AC capacitance scanning probe microscopy. J. Am. Chem. Soc. 130, 887–891.
Menter, T., Haslbauer, J.D., Nienhold, R., Savic, S., Hopfer, H., Deigendesch, N., Frank, S., Turek, D., Willi, N., Pargger, H., Bassetti, S., Leuppi, J.D., Cathomas, G., Tolnay, M., Mertz, K.D., Tzankov, A., 2020. Postmortem examination of COVID-19 patients reveals diffuse alveolar damage with Severe capillary congestion and variegated findings in lungs and other organs suggesting vascular dysfunction. Histopathology 77, 198–209.
Michen, B., Graule, T., 2009. Isoelectric points of viruses. J. Appl. Microbiol. 109, 388–397.
Morgan, H., Hughes, M.P., Green, N.G., 1999. Separation of submicron bioparticles by dielectrophoresis. Biophys. J. 77, 516–525.
Morita, M., Hayashi, K., Horiuchi, T., Shibano, S., Yamamoto, K., Aoki, K.J., 2014. Enhancement of redox cycling currents at interdigitated electrodes with elevated fingers. J. Electrochem. Soc. 161, H178.
Odijk, M., Olthuis, W., Dam, V.A.T., Van Den Berg, A., 2008. Simulation of redox-cycling phenomena at interdigitated array (IDA) electrodes: amplification and selectivity. Electroanalysis 20, 463–468.
Paixão, T.R.L.C., Richter, E.M., Brito-Neto, J.G.A., Bertotti, M., 2006. Fabrication of a new generator-collector electrochemical micro-device: characterization and applications. Electrochem. Commun. 8, 9–14.
Quinn, B.M., Hof, P. G. van't, Lemay, S.G., 2004. Time-resolved electrochemical detection of discrete adsorption events. J. Am. Chem. Soc. 126, 8360–8361.
Rees, N.V., Banks, C.E., Compton, R.G., 2004. Ultrafast chronoamperometry of acoustically agitated solid particulate suspensions: nonfaradaic and faradaic processes at a polycrystalline gold electrode. J. Phys. Chem. B 108, 18391–18394.
Rock, P.A., 1966. The standard oxidation potential of the ferrocyanide-ferricyanide electrode at 25° and the entropy of ferrocyanide ion. J. Phys. Chem. 70, 576–580.
Salm, E., Guevara, C.D., Dak, P., Dorvel, B.R., Reddy, B., Alam, M.A., Bashir, R., 2013. Ultralocalized thermal reactions in subnanoliter droplets-in-air. Proc. Natl. Acad. Sci. U.S.A. 110, 3310–3315.
Sepunaru, L., Plowman, B.J., Sokolov, S.V., Young, N.P., Compton, R.G., 2016. Rapid electrochemical detection of single influenza viruses tagged with silver nanoparticles. Chem. Sci. 7, 3892–3899.
Shieh, W.J., Hsiao, C.H., Paddock, C.D., Guarner, J., Goldsmith, C.S., Tatti, K., Packard, M., Mueller, L., Wu, M.Z., Rollin, P., Su, I.J., Zaki, S.R., 2005. Immunohistochemical, in situ hybridization, and ultrastructural localization of SARS-associated Coronavirus in lung of a fatal case of Severe Acute respiratory Syndrome in Taiwan. Hum. Pathol. 36, 303–309.
Straver, M.G., Odijk, M., Olthuis, W., Van Den Berg, A., 2012. A simple method to fabricate electrochemical sensor systems with predictable high-redox cycling amplification. Lab Chip 12, 1548–1553.
Takamura, K., Fischer, H., Morrow, N.R., 2012. Physical properties of aqueous glycerol solutions. J. Petrol. Sci. Eng. 98–99, 50–60.
Vega-Acosta, J.R., Cadena-Nava, R.D., Gelbart, W.M., Knobler, C.M., Ruiz-García, J., 2014. Electrophoretic mobilities of a viral capsid, its capsid protein, and their relation to viral assembly. J. Phys. Chem. B 118, 1984–1989.
Vishnu, N., Sharma, C.S., Senthil Kumar, A., 2020. A low-cost and miniaturized electrochemical cell for low-sample analyses. Microchem. J. 159, 105591.
Voller, A., Bartlett, A., Bidwell, D.E., Clark, M.F., Adams, A.N., 1976. The detection of viruses by enzyme linked immunosorbent assay (ELISA). J. Gen. Virol. 33, 165–167.
Winkler, T.E., Dietrich, R., Kim, E., Ben-Yoav, H., Kelly, D.L., Payne, G.F., Ghodssi, R., 2017. The interplay of electrode- and bio-materials in a redox-cycling-based clozapine sensor. Electrochem. Commun. 79, 33–36.
Wolfrum, B., Zevenbergen, M., Lemay, S., 2008. Nanofluidic redox cycling amplification for the selective detection of catechol. Anal. Chem. 80, 972–977.
Wolfrum, B., Kätelhön, E., Yakushenko, A., Krause, K.J., Adly, N., Hüske, M., Rinklin, P., 2016. Nanoscale electrochemical sensor arrays: redox cycling amplification in dual-electrode systems. Acc. Chem. Res. 49, 2031–2040.
Xiao, X., Bard, A.J., 2007. Observing single nanoparticle collisions at an ultramicroelectrode by electrocatalytic amplification. J. Am. Chem. Soc. 129, 9610–9612.
Xiao, Y., Fan, F.R.F., Zhou, J., Bard, A.J., 2008. Current transients in single nanoparticle collision events. J. Am. Chem. Soc. 130, 16669–16677.
Xiong, J., Chen, Q., Edwards, M.A., White, H.S., 2015. Ion transport within high electric fields in nanogap electrochemical cells. ACS Nano 9, 8520–8529.
Yan, H., Wu, H., 2008. In: Li, D. (Ed.), Encyclopedia of Microfluidics and Nanofluidics. Springer US, Boston, MA, pp. 886–896.
Zafarani, H.R., Mathwig, K., Sudhölter, E.J.R., Rassaei, L., 2016. Electrochemical redox cycling in a new nanogap sensor: design and simulation. J. Electroanal. Chem. 760, 42–47.
Zhao, Z., Huang, C., Huang, Z., Lin, F., He, Q., Tao, D., Jaffrezic-Renault, N., Guo, Z., 2021. Advancements in electrochemical biosensing for respiratory virus detection: a review. TrAC Trends Anal. Chem. 139, 116253.
Zhu, N., Zhang, D., Wang, W., Li, X., Yang, B., Song, J., Zhao, X., Huang, B., Shi, W., Lu, R., Niu, P., Zhan, F., Ma, X., Wang, D., Xu, W., Wu, G., Gao, G.F., Tan, W., 2020. A novel Coronavirus from patients with pneumonia in China, 2019. N. Engl. J. Med. 382, 727–733.